In-Depth Characterization of Natural Clays from Southeast Albania

Altin Mele [1,2], Viviana Scognamiglio [3], Valeria Nocerino [4], Luca De Stefano [4], Arben Memo [2], Roberta G. Toro [5], Manuela Rossi [6], Francesco Baldassarre [7] and Francesco Capitelli [3,*]

1   Ivodent Academy, Center of Techniques Studies, Rruga Prokop Myzeqari, 1001 Tirana, Albania; altin.mele@ivodent.edu.al
2   Department of Chemistry, University of Tirana, Bulevardi Zog I, 1001 Tirana, Albania; arben.memo@fshn.edu.al
3   Institute of Crystallography, Department of Chemical Sciences and Materials Technologies, National Research Council, Via Salaria Km 29.300, Monterotondo Scalo, 00015 Rome, Italy; viviana.scognamiglio@cnr.it
4   Institute of Applied Sciences and Intelligent Systems, Department of Physical Sciences and Technologies of Matter, National Research Council, Via Pietro Castellino 111, 80131 Naples, Italy; valeria.nocerino@cnr.it (V.N.); luca.destefano@cnr.it (L.D.S.)
5   Institute for the Study of Nanostructured Materials, Department of Chemical Sciences and Materials Technologies, National Research Council, Via Salaria Km 29,300, Monterotondo Scalo, 00015 Rome, Italy; robertagrazia.toro@cnr.it
6   Department of Earth Sciences, Environment and Resources, University of Naples Federico II, Via Cintia, 80126 Naples, Italy; manuela.rossi@unina.it
7   Institute of Crystallography, Department of Chemical Sciences and Materials Technologies, National Research Council, Via Amendola 122/o, 70126 Bari, Italy; francesco.baldassarre@cnr.it
*   Correspondence: francesco.capitelli@cnr.it

Abstract: Clays have been exploited in the manufacture of diverse products from ceramics to paints, pharmaceuticals, plastics, cosmetics, and more. Thus, they can be used in many industrial applications, showing good adsorbent ability thanks to their lamellar structure, high cation exchange capacity, pore size distribution, and large surface area. For this reason, considerable attention has been paid to their in-depth characterization, for further integration in sectors such as biomedicine, construction, remediation, aerospace, and nanotechnology. For this aim, two samples of natural clays, ALO1 and PRE4, from the southeast part of Albania, were subject to a multi-methodological characterization, with the aim of addressing the use of such geomaterials in possible sensing applications. X-ray fluorescence analysis, morphological characterization of the samples, and energy-dispersive system spectroscopy pointed to an extreme mineralogical variety, with kaolinite in AL01 and montmorillonite in PRE4 as the most abundant phases. This fact was further confirmed by powder X-ray diffraction, showing a quartz content of 20%, a kaolinite content of 64%, and a muscovite content of 16% for ALO1; meanwhile, for PRE4, we found a content of quartz of 45%, a content of montmorillonite of 34.9%, and a content of clinochlore of 20%. Infrared spectroscopy and thermal analyses confirmed the presence of hydroxyl groups in both samples, suggesting a higher content in ALO1. Measurement of N_2 adsorption isotherms on the clay samples yields specific surface areas of 87 m^2/g for PRE4 and 32 m^2/g for ALO1, pore volumes of 0.721 cm^3/g for PRE4 and 0.637 cm^3/g for ALO1, and similar pore sizes in the range of 6–12 nm. Electrochemical analysis highlighted a good conductivity of ALO1 and PRE4 when used for the modification of commercial carbon-based screen-printed electrodes. In detail, higher currents were registered by differential pulse voltammetry for the electrodes modified with the clays with respect to bare electrodes, as well as good repeatability of the measurements. In addition, a comparative study with nanomaterials, known for their good conductivity, was achieved, using carbon black and gold nanoparticles as a reference, showing that the conductivity of the clays was lower than but not so different from those of the reference materials.

Keywords: clays; screen-printed electrodes; structural and functional characterization

1. Introduction

Clay minerals, a well-known class of naturally occurring phyllosilicates [1], are attracting considerable attention for the manufacturing of several products with important industrial applications, from water treatment applications to those in the pharmaceutical, automotive, and agriculture industries, among others [2].

Clay minerals, such as the most known montmorillonite $(\frac{1}{2}Ca,Na)(Al,Mg,Fe)_4(Si,Al)_8O_{20}(OH)_4 \cdot nH_2O$, kaolinite $Si_4Al_4O_{10}(OH)_8$, and illite $K_yAl_4(Si_{8-y},Al_y)O_{20}(OH)_4$ (with $1 < y < 1.5$), are characterized by a layered structure that results in high surface area and noticeable ion-exchange capacity [3]. Moreover, they can provide on high chemical stability within harsh environmental conditions, ensuring long-term performance [4]. They are low-cost geomaterials, being naturally abundant and easy to process, and offering a cost-effective solution for developing advanced materials [5]. They are eco-friendly, because they are naturally derived and non-toxic, aligning with the growing demand for environmentally friendly materials [6].

To date, clays have been employed as base material for different kinds of sensors. They show excellent mechanical properties in electrode paste applications [7], and they can be used in gas sensors due to their high adsorption capacity. When gases such as CO_2, NH_3, or volatile organic compounds interact with the clay's surface, changes in electrical resistance or capacitance can be recorded, enabling precise gas sensing [8]. Clays are also enhancing materials for humidity sensors: the hygroscopic nature of clay minerals allows them to absorb and desorb water vapor, which can be monitored through changes in electrical properties. This makes clay-based materials effective for humidity sensing in various environments [9,10]. Clays can also work as electrochemical sensors [7,11,12]. The ion-exchange properties and high surface area of clay minerals enhance the performance of electrochemical sensors for detecting heavy metals, pollutants, and other chemical species in water and soil [13]. Last, they can be exploited as biosensors, where clay minerals can be functionalized with biological molecules (owing to presence in their frameworks of hydroxyl groups [14]), such as enzymes or antibodies, capable of detecting specific target analytes of environmental and biomedical interest [15].

Despite these advantages, the integration of clay minerals into sensing devices presents many challenges. The need for uniform dispersion, compatibility with various transduction mechanisms, and the potential impact of environmental factors on performance require further research. Advances in nanotechnology and material science are expected to address these challenges, enabling the development of more robust and versatile clay-based sensors. In conclusion, clay minerals offer a promising avenue for the advancement of sensor technology. Their unique properties, coupled with ongoing research and development, are set to revolutionize various fields by providing efficient, sustainable, and high-performance sensing solutions. Future research may focus on hybrid systems, combining clay minerals with other nanomaterials (e.g., graphene, metal oxides) to synergistically enhance sensor performance [16], and on innovative techniques, for the functionalization of clay minerals devoted to tailoring their properties for specific sensing applications [10].

In this work, we performed a detailed structural characterization of natural clay samples from southeast Albania (ALO1 and PRE4) by means of X-ray fluorescence, scanning electron microscopy equipped with energy-dispersive system, X-ray diffraction from powder data, and Fourier transform infrared spectroscopy. Thermo- and differential thermogravimetric (TG/DTG) analysis, differential scanning calorimetry (DSC) analysis, adsorption isotherm of gaseous N_2, and pore size distribution complete the characterization.

Afterwards, we provided an electrochemical characterization of both samples to evidence any potential conductivity of the materials. In detail, we exploited the clay samples for the modification of commercial carbon-based screen-printed electrodes and performed differential pulse voltammetry (DPV) analysis of the modified electrodes. Such clay-modified electrodes were finally compared to bare ones and to electrodes nanomodified with nanomaterials known for their good conductivity. In particular, carbon black and gold nanoparticles were used as reference nanomaterials.

2. Materials and Methods

2.1. Geological Occurrence and Pretreatment of Clays Samples

The sample AL01 was collected in the Alarup coal mine in southeast Albania (Figure 1). It belongs to Cerrave conglomerates of continental lacustrine and fluvial–deltaic sediments, which are formed through the intercalation of coal–clay lenses with dominant sand and gravel contents. The clay mineral PRE4 sample originates from Prrenjas, Albania (Figure 1); it was reported on in [17,18], where it was preliminarily described as bentonite, mainly made up of smectite with quartz and illite impurities, formed from the alteration of ultra-basic rocks that are rich in magnesium; this was deposited in lagoons during the Holocene times after transport and sedimentation from the mountain.
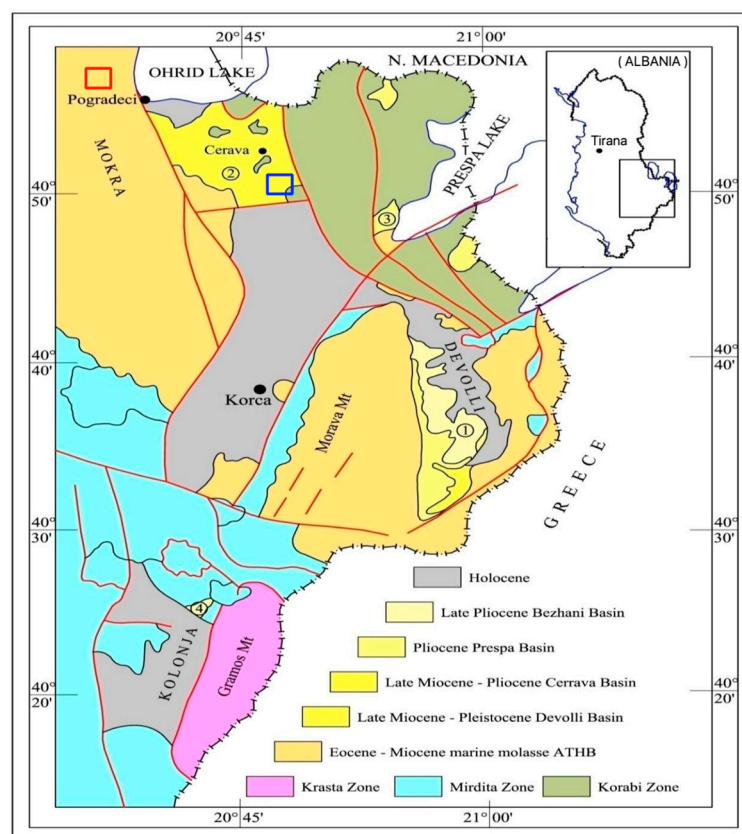

Figure 1. Geological map of southeastern Albania showing the Neogene basins (modified after Geological Map 1:200,000 of Albania): 1—Devolli Basin; 2—Alarup-Cerava Basin; 3—Prespa Basin; 4—Bezhani Basin; (B-inset) location of the area in the map of Albania (adapted from [18]). Red rectangle—sampling area of ALO1 (Alarup region); blue rectangle—sampling area of PRE4 sample (Prrenjas region).

Both the samples were collected at a depth of around 20 cm, avoiding grass, plants, and roots on the immediate ground surface. Clay samples were first grounded and sieved to less than 0.1 mm, then washed from impurities by precipitation of its coarse fraction in deionized water out of a clay mineral suspension of 10% (mass/volume). The washing occurred inside of glass bottles of 3 L volume, leaving a coarse mineral–precipitate fraction for 5 min, and collecting the clay colloidal solution through a glass valve, 5 cm from the bottom. This procedure was repeated three times in three different glass bottles and the collected clay suspension was dried overnight in a lab drier at 105 °C.

2.2. X-Ray Fluorescence Analysis

X-ray fluorescence (XRF) chemical analyses were conducted by a high-performance wavelength dispersive XRF spectrometer, Bruker ASX S8 Tiger Series 2 (±0.00005) (Bruker

Scientific, Billerica, MA, USA); the smallest spot size for sample mapping was 300 μm; the excitation current was 170 mA. The experimental data were processed with SPECTRA plus v3 Software Package for X-ray Spectrometers (Bruker Scientific, Billerica, MA, USA).

2.3. Optical Microscopy and Energy-Dispersive System Spectroscopy

The microscope that was used for morphological and mineralogical characterization of the thin section samples was the Axio Imager A1m by Zeiss (powered by the Museum Center of Natural and Physical Sciences, Federico II University, Naples, Italy). The AxioCam ICc5 camera (ZEISS, Oberkochen, Germany) was used for image acquisition; the software Axiovision SE64 Version 4.9.1 with Automeasure module was employed.

Quantitative chemical analyses of thin-section samples were performed by using a scanning electron microscope (SEM) JEOL-JSM 5310 (JEOL, Tokyo, Japan) at CISAG, University of Naples Federico II, coupled with energy-dispersive X-ray spectroscopy (EDS). The setup is equipped with an Oxford Instruments Microanalysis unit: INCA X-act detector and operating at 15 kV primary beam voltage, 50–100 mA filament current, variable spot size, 20 mm WD, and 40 s real-time net acquisition. INCA X-act detector uses Energy 350 software with an XPP matrix correction scheme and Pulse Pile-up correction. The data were processed with dedicated software INCA software version 4.08 (Oxford Instruments, Abingdon, UK). Natural and synthetic materials were used as standards: wollastonite for Si and Ca; phlogopite for F; KCl for Cl; jadeite for Na; barite for S; celestine for Sr; olivine for Fe; pericline for Mg; orthoclase for K; corundum for Al; Mn (metallic) for Mn; rutile for Ti. For quantitative chemical analyses, the samples were coated with graphite. A total of 10 analytical points for each minerals sample were collected; 5 crystals were analyzed for each mineral.

2.4. Preparation of Clay Suspensions and Clay-Modified SPEs

A suspension was obtained dissolving the clays in distilled water and ethanol in a ratio 1:1 (*v/v*), at a final concentration of 1 mg/mL. The suspension was sonicated using the Hielscher UP200St-Ultrasonic Transducer (200 W, 26 kHz, 30 min) and then used for the functionalization of the working electrode (WE) of a commercial carbon-based screen-printed electrode (SPE).

Carbon black (CB) and gold nanoparticles (AuNPs) were used as reference nanomaterials. CB (type N220) was kindly provided by the group of Prof. Fabiana Arduini of Tor Vergata University (Rome, Italy) [19]. The nanoparticles measured 10–20 nm in diameter. AuNPs were kindly provided by the group of Dr. Luca De Stefano of ISASI-CNR (Naples, Italy) [20]. The nanoparticles measured ca. 200 nm in diameter.

The WE of the SPEs was modified by drop casting using different volumes of the 1 mg/mL clay suspension as well as 1 mg/mL CB and AuNPs suspensions, covering all the WE area, which has a diameter of 4 mm. The SPEs (screen-printed carbon electrodes; 110—DropSens110) were purchased from DropSens (Asturias, Spain, dropsens.com), comprising three electrode systems with an Ag reference electrode, a graphite counter, and working electrodes.

2.5. Electrochemical Characterization

The electrochemical properties of the SPEs modified with the clays and the reference nanomaterials (CB and AuNPs) were evaluated by differential pulse voltammetry (DPV) in comparison with bare SPEs. In DPV analysis. The parameters were set as follows: E begin: -0.2 V; E end: 0.4 V; E step: 0.01 V; E pulse: 0.2 V; T pulse: 0.02 s; scan rate: 0.01 V/s. The measurements were performed using a solution of 0.1 M KCl, 5 mM $K_3Fe(CN)_6$/$K_4Fe(CN)_6$ in a ratio 1:1 (*v/v*). The electrochemical analyses were carried out using a PalmSens4 potentiostat (PalmSens, Houten, The Netherlands, palmsens.com).

2.6. Powder X-Ray Diffraction

Powder X-ray diffraction (PXRD) analyses were carried out using a Rigaku Smartlab SE (Rigaku, Tokyo, Japan) diffractometer operating with a Cu Kα radiation anode at 40 kV and 30 mA, and equipped with a silicon strip Rigaku D/teX Ultra 250 detector. Data were collected over the 2θ range of 5–80° at a rate of 1° min^{-1} and with a 0.01° step resolution. PXRD data were also qualitatively analyzed through SmartLab Studio II softwareversion v4.6.426.0 (Rigaku, Tokyo, Japan), based on the use of the free POW_COD database [21].

2.7. Infrared Spectroscopy

FTIR spectra were achieved by using a Nicolet iS50 FT-IR Spectrometer instrument (Thermo Scientific, Waltham, MA, USA), within the 525–4000 cm^{-1} frequency range and with a resolution of 4 cm^{-1}. The instrument was equipped with an attenuated total reflectance (ATR) diamond crystal accessory for data acquisition. In order to acquire the FTIR spectra of both clay samples, pertinent powder samples were used without any prior treatment.

2.8. Thermogravimetric (TG), Differential TG, and Scanning Calorimetry Analysis

The thermogravimetric and differential calorimetric thermal analysis were performed simultaneously in a STA 449 F5 Jupiter instrument (Netzsch, GB, Selb, Germany) in the temperature range from 30 to 1000 °C, at a heating rate 10 K/min, in an Al_2O_3 crucible without lead, under N_2 purge gas 20 mL/min. The sample amounts were approximately 50 mg, and the calorimeter was calibrated using different metals in the temperature range from room temperature up to 1200 °C. The measurement results were evaluated using the dedicated software NETZSCH—Thermal Analysis—Version 8.0.3 (NETZSCH—GeraetebauGmbh, Selb/Bayern, Germany).

2.9. Adsorption Isotherm of Gaseous N_2 and Pore Size Distribution

The adsorption of gaseous N_2 at T = 77 K was performed using a Sorptomatic 1900 instrument of Carlo Erba manufacturer (Emmendingen, Germany). Samples of approximately 1 g were first degassed for 2 h at 200 °C under a vacuum of 3 Pa. For the evaluation of the results out of adsorption isotherms were used the BET model for the evaluation of specific surface area, the Gurvitch rule for the determination of the cumulative pore volume and Kelvin equation to calculate the mesopore size distribution.

3. Results and Discussion

3.1. Chemical and Morphological Studies

Table 1 reports the results (wt%) of XRF analysis on clay samples: values are provided with standard deviations (SDs, determined by several errors, mainly the errors in sample preparation, σSP, the instrumentation error, σInst, and the counting statistics error, σCSE). Table 2 reports details on the mineral composition, the background mass, and the clast size of ALO1 and PRE4 samples, while Table 3 reports EDS chemical analyses of most abundant phases (over quartz) in both the samples. Figure 2 presents the optical microscope images (20×) of ALO1 and PRE4 (parallel nicols mode). Morphological analyses (Figure 2) show a pronounced difference among the two clay samples. In ALO1, there is a microcrystalline background mass in which there are several clasts of different sizes, made by quartz, feldspars, and iron hydroxides. From a chemical point of view, EDS analyses (Table 2) highlighted the presence of kaolinite, with significant FeO values (FeO ranging from 0.5 to 2.2 wt%), of muscovite (ideally $KAl_2(Si_3Al)O_{10}(OH,F)_2$), with FeO values between 1.52 and 9.04 wt%, and a low amount of montmorillonite. In PRE4, there is a cryptocrystalline background mass made by crystals of different dimensions, mainly represented by quartz and feldspar. Chemical analyses showed the occurrence of smectite group minerals on all the montmorillonite–vermiculite mixtures; additionally, they highlighted the presence of chlorite group minerals, in particular the isomorphous mixture chamosite–clinochlore.

Table 1. XRF measurements (wt%) of investigated clay samples.

	ALO1	**PRE4**	**SD (%)**
SiO$_2$	47.888	50.512	0.280
Al$_2$O$_3$	22.244	9.211	0.100
Fe$_2$O$_3$	10.910	13.285	0.034
CaO	0.710	0.634	0.310
MgO	0.847	4.274	0.160
K$_2$O	1.616	0.524	0.089
Na$_2$O	0.228	0.372	0.036
TiO$_2$	1.192	0.539	0.022
P$_2$O$_5$	0.171	0.039	0.003
MnO	0.216	0.076	0.003
Cr$_2$O$_3$	0.049	0.526	0.002
LOI *	13.1	19.7	-
Total	*99.2*	*99.7*	-

* LOI = Loss on ignition is measured by thermogravimetric analysis.

Table 2. Details on the background mass, on the clasts size, and on the mineralogical composition of the investigated clay samples.

	Background Mass	*Clast Size*	*Mineral Composition*
ALO1	2.5 μm	35 μm	Quartz, kaolinite, muscovite; labradorite, K-feldspar; iron hydroxide
PRE4	-	17 μm	Quartz, montmorillonite–vermiculite; labradorite, albite, sanidine, chamosite–clinochlore

Table 3. EDS chemical analyses of most abundant phases (over quartz) in ALO1 and PRE4 samples.

	ALO1		**PRE4**	
	Kaolinite	Muscovite	Montmorillonite	Chamosite/Clinochlore
MgO	-	2.43 (20)	4.10 (25)	10.52 (15)
Al$_2$O$_3$	39.32 (20)	32.41 (22)	10.72 (55)	10.97 (54)
SiO$_2$	45.32 (5)	46.28 (51)	46.62 (95)	30.25 (1.2)
K$_2$O	0.10 (1)	8.63 (15)	0.45 (15)	0.31 (15)
CaO	0.11 (5)	-	0.57 (12)	1.18 (10)
TiO$_2$	-	0.07 (1)	0.23 (25)	-
MnO	-	-	0.06 (1)	4.45 (3.5)
FeO	1.26 (15)	5.43 (22)	15.32 (30)	30.78 (4.2)
Total	86.11	95.25	78.06	88.46
H$_2$O	13.89	4.75	21.94	11.55

The mineralogical variability of the samples was confirmed by XRF analysis (Table 1) carried out on the whole samples. Particularly, the higher Al$_2$O$_3$ content in ALO1 (22.244 wt%), compared to PRE4 (9.211 wt%), is mainly attributed to the presence of phases such as kaolinite and muscovite. The higher content of K$_2$O in ALO1 (1.616 wt%), compared to PRE4 (0.524 wt%), is due to the presence of muscovite. Similarly, the higher amount of MgO in PRE4 (4.274 wt%), compared to ALO1 (0.847 wt%), is due to the occurrence of montmorillonite and chamosite/clinochlore.
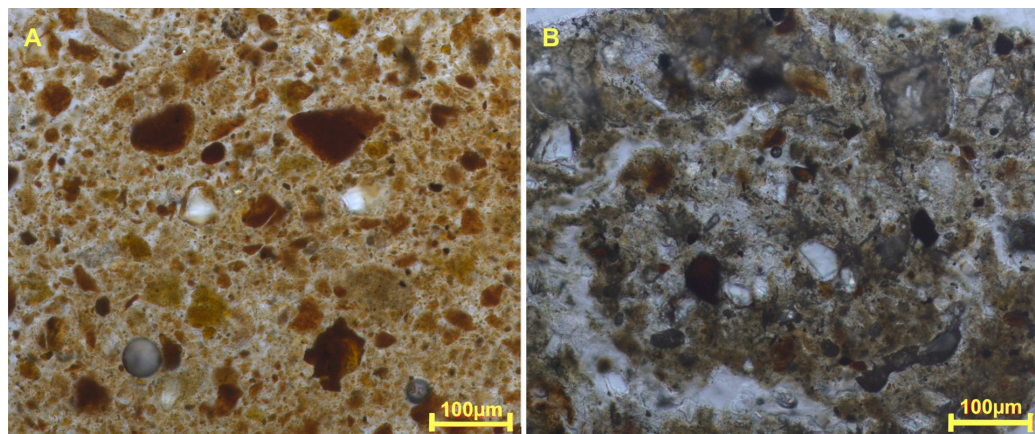
Figure 2. Optical microscope images (20×) of ALO1 (**A**) and PRE4 (**B**) samples in thin sections (parallel Nicols mode).

3.2. Electrochemical Characterization

DPV analyses were conducted on bare SPEs as well as on SPEs modified with 1 mg/mL PRE4 and ALO1 (obtained as described in Section 2.4), for the evaluation of the clay's potential conductivity. Also, CB and AuNPs nanomodified SPEs were tested as reference, using a suspension of each nanomaterial at a final concentration of 1 mg/mL. Each SPE was considered as a disposable system and three different SPEs were used to evaluate the repeatability of the measurements.

As reported in Figure 3, different amounts of the clays were used for the modification of the SPEs, e.g., 2, 4, and 6 μL of a suspension with a final concentration of 1 mg/mL, to determine the optimum amount of the material to be used for the electrode modification. For PRE4 modified SPEs, a current with 4 μL higher than 2 and 6 μL was obtained. Thus, all the further analysis were conducted using 4 μL of PRE4. For ALO1, 4 μL were also chosen for all subsequent analyses, since the corresponding current was higher than that of 2 μL and similar to that of 6 μL, but with a lower standard deviation. A good repeatability of the measurements was obtained ($n = 3$).

DPV analysis was then performed on clay-modified SPEs in comparison to bare SPEs and SPEs nanomodified with CB and AuNPs (4 μL of a 1 mg/mL suspension of clay, CB, and AuNPs were used). This comparative study highlighted that the conductivity of PRE4 and ALO1 was higher than that of the bare SPEs (Figure 4), and lower but not so far from those of the reference materials, carbon black and gold nanoparticles. Also, in this case, a good repeatability of the measurements was obtained ($n = 3$).
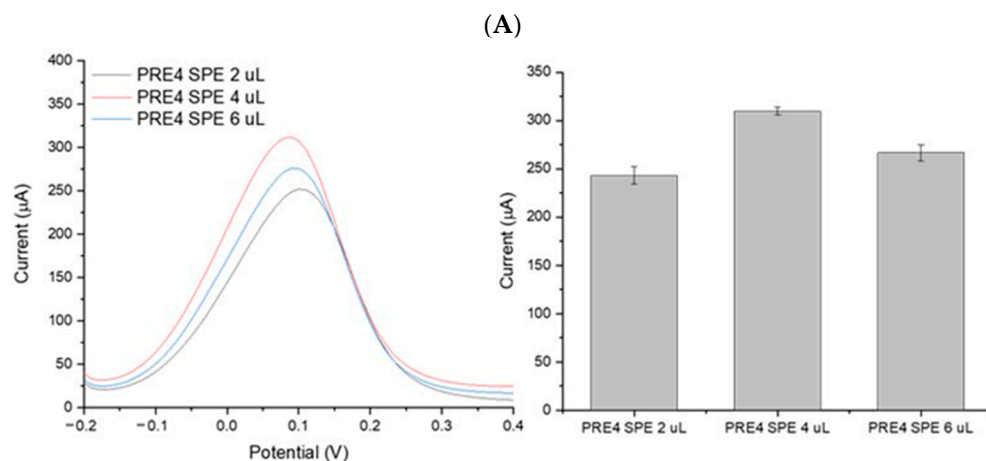
(A)

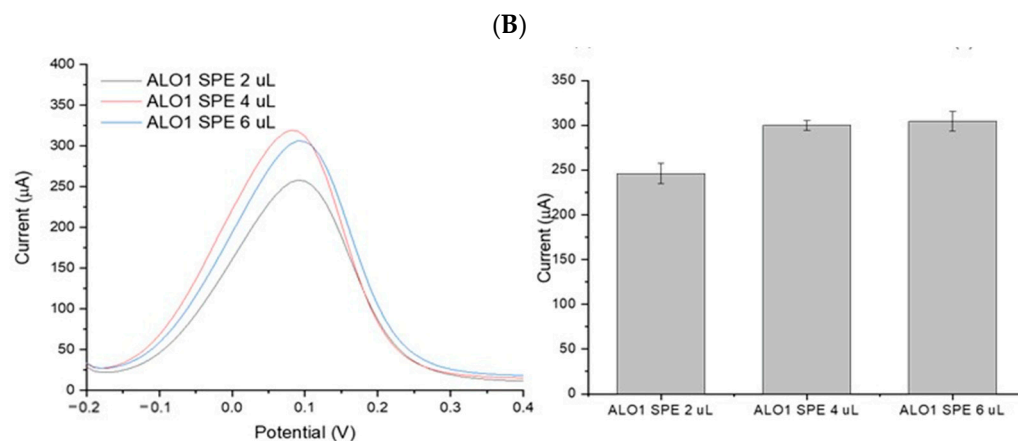**Figure 3.** *Cont.*

Figure 3. Electrochemical characterization of PRE4-modified SPEs (**A**) and ALO1-modified SPEs (**B**) by DVP using 0.1 M KCl, 5 mM $K_3Fe(CN)_6/K_4Fe(CN)_6$ as the electrochemical mediator (n = 3). SPE—screen-printed electrode; SPE-PRE4—modified with PRE4; SPE-ALO1—modified with ALO1.
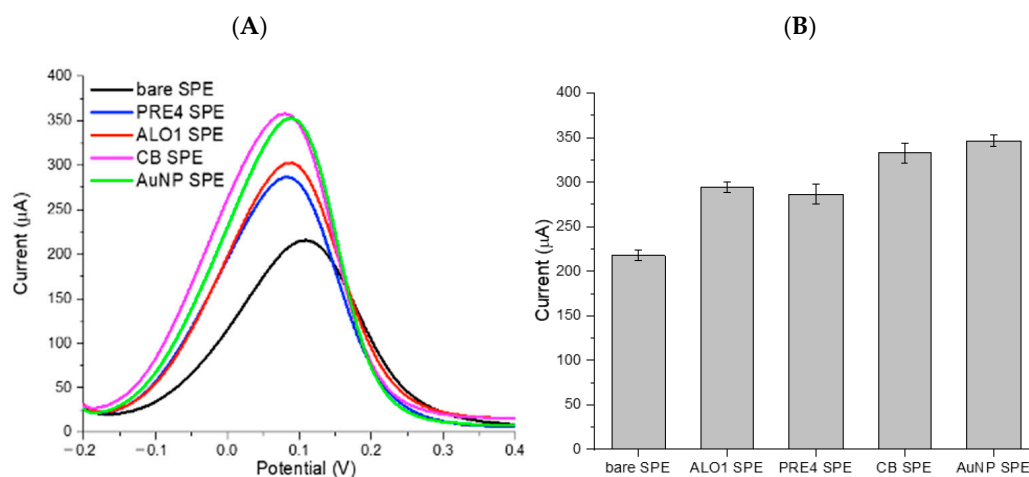

Figure 4. Electrochemical characterization of bare SPEs, clay-modified SPEs, CB-SPEs, and AuNPs SPEs by DVP using 0.1 M KCl, 5 mM $K_3Fe(CN)_6/K_4Fe(CN)_6$ as the electrochemical mediator (n = 3): (**A**) DPV spectra and (**B**) Histogram reporting current values at the maximum peak for 3 electrode with standard deviation. SPE—screen-printed electrode; SPE-PRE4—modified with PRE4; SPE-ALO1—modified with ALO1; SPE-CB—modified with carbon black nanoparticles; SPE-AuNPs—modified with gold nanoparticles.

DPV analysis was also conducted on the same SPE before and after modification with the clays. The SPE was modified with 4 µL of 1 mg/mL of PRE4 and ALO1 and tested before and after the functionalization. As reported in Figure 5, the results confirmed the data depicted in Figure 4, as the presence of both PRE4 and ALO1 used for SPE modification were able to enhance the conductivity of the electrode.
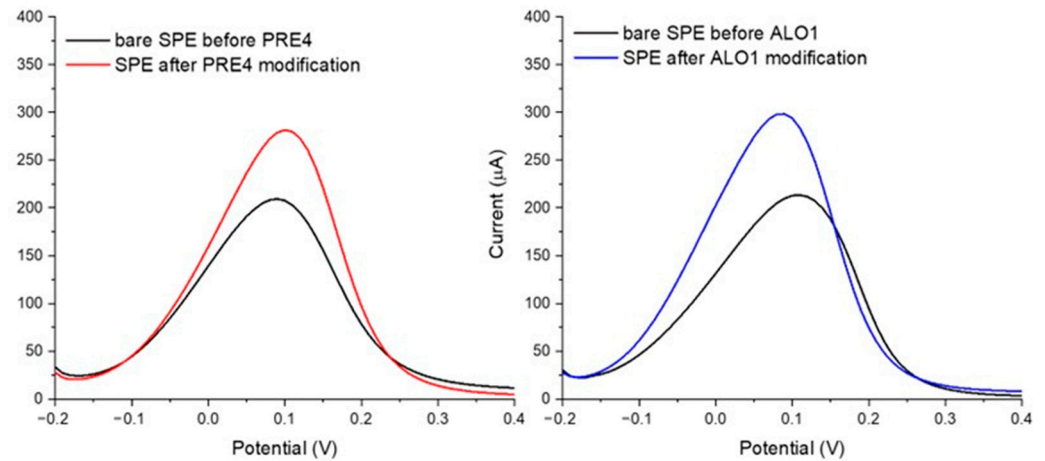
Figure 5. Electrochemical characterization of a SPE before (black) and after PRE4 (red) and ALO1 (blue) modification by DVP using 0.1 M KCl, 5 mM $K_3Fe(CN)_6/K_4Fe(CN)_6$ as the electrochemical mediator. SPE—screen-printed electrode.

3.3. X-Ray Diffraction Characterization

Interpretation of XRD patterns (Figure 6) show that ALO1 sample has strong peaks of kaolinite, and low-intensity peaks assigned to quartz, muscovite, and montmorillonite. The intense and sharp peaks of kaolinite, e.g., those at $2\theta = 12.36°$ and $20.86°$, reveal an ordered structure of this phyllosilicate [22]. Muscovite shows a characteristic peak at $2\theta = 8.88°$ [23]. The quartz strongest peak is at $2\theta = 26.65°$; moreover, this is the strongest peak of the pattern. A different scenario arises in PRE4 sample, where quartz and, most significantly, montmorillonite are present; the occurrence of the latter is indicated by the diffraction peak at $2\theta = 5.90°$ [24], instead of muscovite. In this regard, semiquantitative analyses of the mineralogical phases, achieved according to the results of X-ray diffraction as shown in Figure 4, indicate that the analyzed clays, for ALO1 sample, are composed of quartz at 20%, kaolinite at 64%, and muscovite at 16; meanwhile, the PRE4 sample contains 45% quartz, 34.9% montmorillonite, and 20% clinochlore.
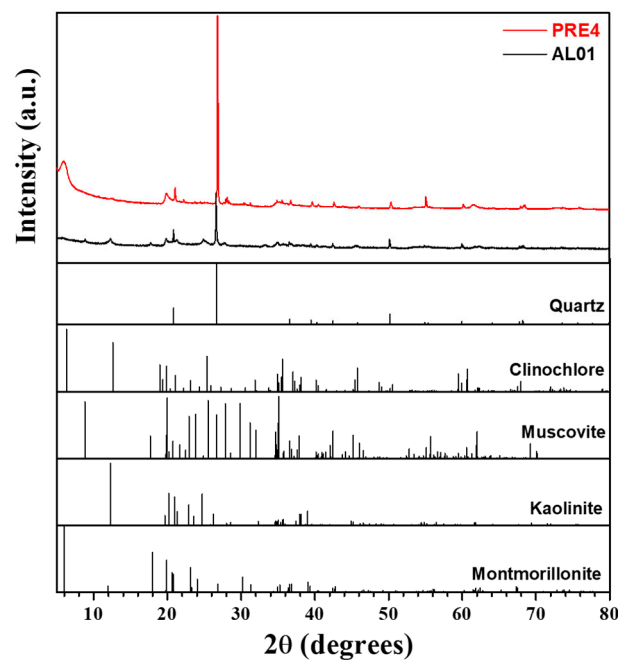

Figure 6. Powder XRD spectra of investigated clay samples.

3.4. FTIR Investigation

FTIR vibrational spectroscopy is widely used in clay minerals characterization, owing to its stability in volatile and light elements detection environments [25,26]. Accordingly, FTIR spectroscopic investigations of clay samples have been reported for a long time in the literature [27–34]. On these bases, the FTIR spectra of the present clay powders were collected in the 400–4000 cm^{-1} wavenumber region; these are reported in Figure 7. Experimental band positions (wavenumbers, cm^{-1}) are provided in Table 4.
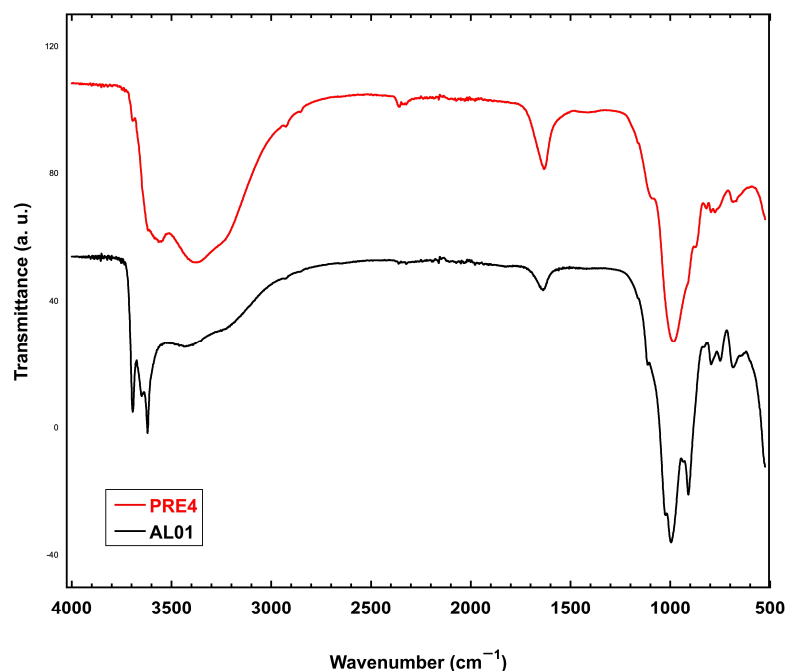
Figure 7. FTIR spectra of ALO1 and PRE4 clay samples in the 4000–400 cm^{-1} region.

Table 4. Experimental absorptions in the IR spectra with assignments for present clay samples.

ALO1	Assignment	PRE4	Assignment
3696 3670 w 3651 3619	ν_s(OH)	3697 3623 3400 3626 w	ν_s(OH)
1634	δ_s(H$_2$O)$_{mont}$	1637	δ_s(H$_2$O)$_{mont}$
1112 1026 996	ν_s(Si-O)	1113 1035 w 985	ν_s(Si-O)
909	ν_s(Al-OH)	915 873 836	ν_s(Al-OH)
795 749	ν_s(Si-O-Al)	801 770	ν_s(Si-O-Al)
685	ν_s(Al-OH)		ν_s(Al-OH)

w = weak.

In the FTIR spectrum (Figure 4) of ALO1 sample, the characteristic bands of kaolinite were identified. The absorption bands between 3500 and 3750 cm^{-1} correspond to the stretching frequencies of OH groups [31]; in particular, the four well-defined characteristic bands at 3696, 3670, 3651, and 3619 cm^{-1} are reliable indicators of an ordered structure of kaolinite [32]. On the other hand, if there is a loss of the higher band, 3670 cm^{-1}, according

to [32], the kaolinite structure is disordered, with a tendency toward dehydration; this is in good agreement with data from the thermogravimetric analysis conducted here. Regions lower than 1112 cm^{-1} belong to the stretching frequencies of SiO$_4$ or AlO$_4$ tetrahedra. At 1635 cm^{-1}, we can appreciate the bending vibration of water that is characteristic of montmorillonite [33]; here, we witnessed its occurrence and thus confirmed the results of the XRD analysis. The group of intense emissions at 1116, 1026, and 996 cm^{-1} are typical of Si-O bonds, while those at 939 and 909 cm^{-1} are characteristic of Al-OH bonds. At 789 and 754 cm^{-1}, we have bonds made by bridging the oxygens of the tetrahedral (SiO$_4$) and octahedral (AlO$_4$) layers of kaolinite. Lastly, at 685 cm^{-1}, we see an Al-OH bond.

The FTIR spectrum of PRE4 clay sample is characterized by an absorption band at about 3623 cm^{-1}, due to the stretching vibrations of structural OH groups, which is typical of montmorillonite [34]. The bands corresponding with the AlAlOH and AlMgOH bending vibrations were observed at 915 and 836 cm^{-1}, respectively. The complex band at 1035 cm^{-1} is due to the stretching vibrations of Si–O groups (signaled at 1013 cm^{-1} in clinochlore by [29]). Water in montmorillonite gives a broad band at about 3420–3450 cm^{-1}, corresponding with the H$_2$O stretching vibrations. The shoulder that is close to 3330 cm^{-1} is due to an overtone of the bending vibration of water observed at 1637 cm^{-1} [33]. A weak peak at 692 cm^{-1} is due to the occurrence of quartz [30].

3.5. Thermogravimetric and Differential Scanning Calorimetry Analysis

In the investigation of the clays, thermal analysis was used to understand the changes occurring during the thermal treatments at different temperatures, and is also used in evaluating their composition. The thermogravimetric analysis shows that the water removal is similar in both of the clay minerals (Figures 8 and 9) and happens until 300 °C. In the case of the kaolinitic clay mineral AL01, we observe two peaks of dehydration at 76.9 °C and 157.1 °C. The first one shows the release of water from interaggregate spaces and the second peak shows water released from the hydration sphere of the cations, as described in the literature [35]. For the other sample, PRE4, the water release is present as a smooth peak from room temperature up to 300 °C for intercalated, adsorbed, and cation hydration water.
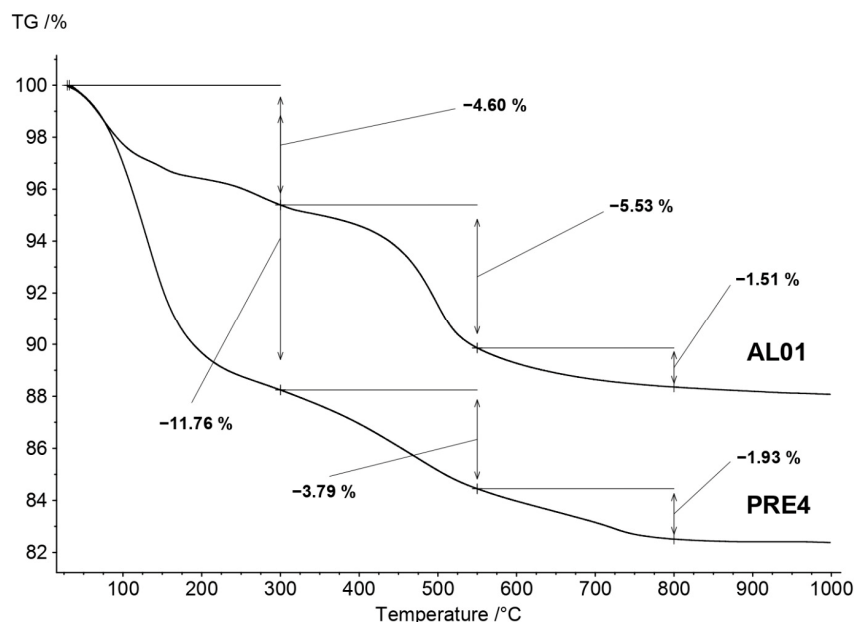

Figure 8. Thermogravimetric curves of clay mineral samples AL01 and PRE4.
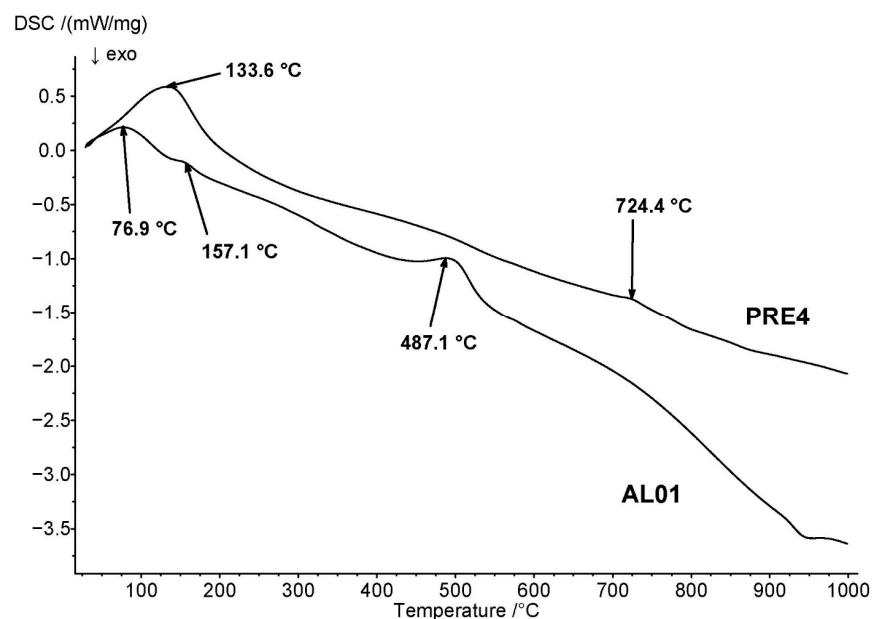
Figure 9. Differential scanning calorimetry curves of clay mineral samples AL01 and PRE4.

For the AL01 sample, the dehydroxylation peak is observed at 487.1 °C, as reported in Figure 8; this is typical for kaolinitic minerals [36], which, according to [37], when endothermic and lower than 530 °C, corresponds to a very disordered kaolin. This suggestion is supported by the pore size distribution of AL01, as shown in Figure 9, where the agglomerates of the sample correspond to the most frequent pore sizes at around 6–12 nm. On the other hand, for the sample PRE4 of high montmorillonite content, the dehydroxylation process is presented by the peak at 724.4 °C, as described in the literature [35]. The mass loss corresponding mainly to dehydroxylation and ranging from 300 °C to 750 °C is higher in the AL01 sample (7.04%) compared to the PRE4 sample (5.72%).

3.6. Adsorption Isotherms of Gaseous N_2, Pore Size Distribution

In Figure 10, the N_2 adsorption isotherms at T = 77 K on AL01 and PRE4 clay samples are shown. Out of these measurements and using the BET model, the specific surface areas of the clay minerals were calculated, as shown in Table 5. Measuring the amount of condensed N_2 moles inside the pores at $p \approx 950$ mbar (second Gurvitch Rule), the cumulative pore volume of the samples was determined. Both the specific surface area and the pore volume are higher in the case of the PRE4 sample. The pore size distribution reported in Figure 11 shows a similar pattern in both cases. The most frequent pore sizes are between 6 and 12 nm. These sizes correspond to the spaces created in between particles of clay which hold together by adhesion. The high surface and pore volume are important surface parameters when the clays are used as electrode pastes, because the adsorption of differently charged species from the solution depends on them.

Table 5. Surface parameters of clay mineral samples AL01 and PRE4 as calculated from N_2 adsorption measurements at T = 77 K, BET model, and Gurvitch Rule.

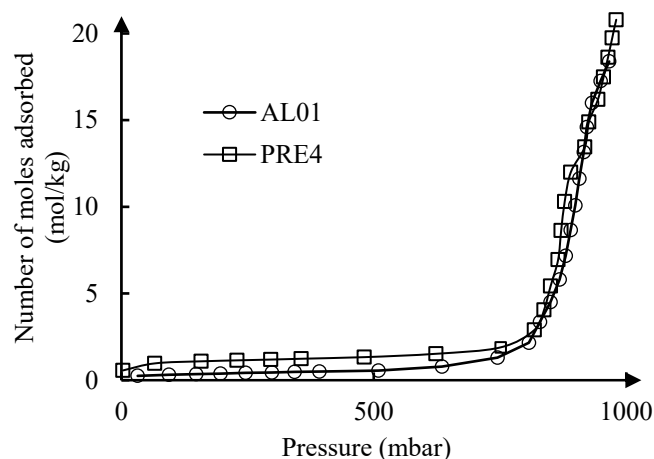| Sample	Surface Area (m²/g)	Pore Volume Vp (cm³/kg)
AL01	32	637
PRE4	87	721

Figure 10. Adsorption isotherms of gaseous N_2 at T = 77 K on clay mineral samples AL01 and PRE4.
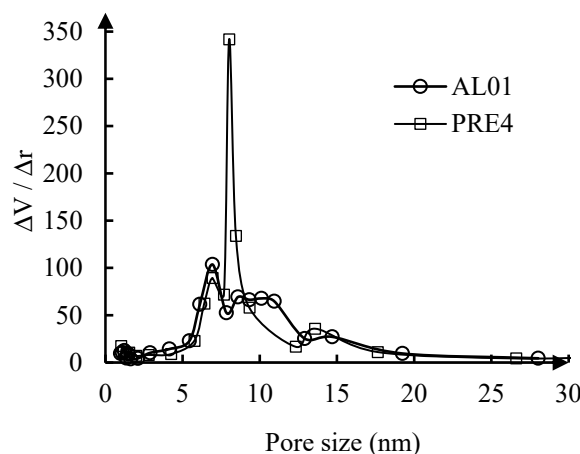

Figure 11. Pore size distribution of clay mineral samples AL01 and PRE4.

4. Conclusions

In this study, an in-depth characterization of clay samples PRE4 and ALO1 was carried out to shed light on the morphological, structural, and electrochemical features of such an astonishing material which has numerous potential industrial applications.

The morphological characterization of the samples, based on optical microscopy, highlighted large surface area of clay particles. Thermogravimetric analyses highlighted a mass loss corresponding mainly to dehydroxylation in the AL01 sample compared to the PRE4 sample, suggesting a higher content of hydroxyl groups in the AL01 sample. The adsorption isotherms of gaseous N_2 suggested that the specific surface area and pore volume were higher in the case of the PRE4 sample. The pore size distribution report, for both the samples, showed that the most frequent pore sizes had values of 6–12 nm: these sizes correspond to the interstitial spaces of clays, which hold together by adhesion. The high surface and pore volume are important surface parameters when the clays are used as electrode pastes, because the adsorption of different charged species from the solution depends on them.

The structural characterization, based on X-ray diffraction and on FTIR spectroscopy, converged to the polyphasic nature of both the samples, with the predominance of kaolinite in ALO1 and montmorillonite in PRE4.

DPV analyses described a higher conductivity of the clay-modified SPEs in comparison to bare electrodes and a conductivity that was lower but not very different from those of the SPEs that were nanomodified with CB and AuNPs, used as the known reference nanomaterials.

References

1. Barcelos, I.D.; de Oliveira, R.; Schleder, G.R.; Matos, M.J.S.; Longuinhos, R.; Ribeiro-Soares, J.; Barboza, A.P.M.; Prado, M.C.; Pinto, E.S.; Gobato, Y.G.; et al. Phyllosilicates as earth-abundant layered materials for electronics and optoelectronics: Prospects and challenges in their ultrathin limit. *J. Appl. Phys.* **2023**, *134*, 090902. [CrossRef]
2. Kalendova, A.; Kupkova, J.; Urbaskova, M.; Merinska, D. Applications of Clays in Nanocomposites and Ceramics. *Minerals* **2024**, *14*, 93. [CrossRef]
3. Kumari, N.; Chandra, M. Basics of Clay Minerals and Their Characteristic Properties. In *Clay and Clay Minerals*; IntechOpen: London, UK, 2021. [CrossRef]
4. Lan, Y.; Liu, Y.; Li, J.; Chen, D.; He, G.; Parkin, I.P. Natural Clay-Based Materials for Energy Storage and Conversion Applications. *Adv. Sci.* **2021**, *8*, e2004036. [CrossRef] [PubMed]
5. Lazaratou, C.V.; Vayenas, D.V.; Papoulis, D. The role of clays, clay minerals and clay-based materials for nitrate removal from water systems: A review. *Appl. Clay Sci.* **2020**, *185*, 105377. [CrossRef]
6. La Noce, M.; Lo Faro, A.; Sciuto, G. Clay-Based Products Sustainable Development: Some Applications. *Sustainability* **2021**, *13*, 1364. [CrossRef]
7. Skowron, E.; Spilarewicz-Stanek, K.; Guziejewski, D.; Koszelska, K.; Metelka, R.; Smarzewska, S. Analytical Performance of Clay Paste Electrode and Graphene Paste Electrode-Comparative Study. *Molecules* **2022**, *27*, 2037. [CrossRef]
8. Wang, L.; Cheng, J.; Jin, Z.; Sun, Q.; Zou, R.; Meng, Q.; Liu, K.; Su, Y.; Zhang, Q. High-pressure hydrogen adsorption in clay minerals: Insights on natural hydrogen exploration. *Fuel* **2023**, *344*, 127919. [CrossRef]
9. Xu, Y.; Liu, S.; Zhang, J.; Chai, S.; Li, J.; Xue, C.; Wu, S. Fabrication of Micro-Cantilever Sensor Based on Clay Minerals for Humidity Detection. *Sensors* **2023**, *23*, 6962. [CrossRef]
10. Guth, U.; Brosda, B.; Schomburg, J. Applications of clay minerals in sensor techniques. *Appl. Clay Sci.* **1996**, *11*, 229–236. [CrossRef]
11. Mousty, C. Sensors and biosensors based on clay-modified electrodes—New trends. *Appl. Clay Sci.* **2004**, *27*, 159–177. [CrossRef]
12. Mousty, C. Biosensing applications of clay-modified electrodes: A review. *Anal. Bioanal. Chem.* **2010**, *396*, 315–325. [CrossRef] [PubMed]
13. Khan, S.; Ajmal, S.; Hussain, T.; Ur Rahman, M. Clay-based materials for enhanced water treatment: Adsorption mechanisms, challenges, and future directions. *J. Umm. Al-Qura Univ. Appll. Sci.* **2023**, *9*. [CrossRef]
14. Smutok, O.; Katz, E. Biosensors: Electrochemical Devices-General Concepts and Performance. *Biosensors* **2022**, *13*, 44. [CrossRef] [PubMed]
15. Fomina, M.; Skorochod, I. Microbial Interaction with Clay Minerals and Its Environmental and Biotechnological Implications. *Minerals* **2020**, *10*, 861. [CrossRef]
16. Mylarappa, M.; Raghavendra, N.; Bhumika, N.R.; Chaithra, C.H.; Nagalaxmi, B.N.; Shravana Kumara, K.N. Study of ZnO nanoparticle-supported clay minerals for electrochemical sensors, photocatalysis, and antioxidant applications. *ChemPhysMater* **2024**, *3*, 83–93. [CrossRef]
17. Jozja, N.; Baillif, P.; Touray, J.C.; Pons, C.H.; Muller, F.; Burgevin, C. Impacts «multi-échelle» d'un échange (Mg,Ca)-Pb et ses conséquences sur l'augmentation de la perméabilité d'une bentonite: Multiscale impacts of a (Mg,Ca)-Pb exchange on the permeability increase of a bentonite. *Comptes Rendus Geosci.* **2003**, *33*, 729–736. [CrossRef]
18. Pashko, P.; Aliaj, S. Stratigraphy and Tectonic Evolution of Late Miocene-Quaternary Basins in Eastern Albania: A Review. *Bull. Geol. Soc. Greece* **2020**, *56*, 317–351. [CrossRef]

19. Mazzaracchio, V.; Tomei, M.R.; Cacciotti, I.; Chiodoni, A.; Novara, C.; Castellino, M.; Arduini, F. Inside the different types of carbon black as nanomodifiers for screen-printed electrodes. *Electrochim. Acta* **2019**, *317*, 673–683. [CrossRef]

20. Bastús, N.G.; Comenge, J.; Puntes, V. Kinetically controlled seeded growth synthesis of citrate-stabilized gold nanoparticles of up to 200 nm: Size focusing versus Ostwald ripening. *Langmuir* **2011**, *27*, 11098–11105. [CrossRef]

21. Altomare, A.; Corriero, N.; Cuocci, C.; Falcicchio, A.; Moliterni, A.; Rizzi, R. QUALX2.0: A Qualitative Phase Analysis Software Using the Freely Available Database POW_COD. *J. Appl. Crystallogr.* **2015**, *48*, 598–603. [CrossRef]

22. Aparicio, P.; Galan, E. Mineralogical interference on kaolinite crystallinity index measurements. *Clays Clay Miner.* **1999**, *47*, 12–27. [CrossRef]

23. Gridi-Bennadji, F.; Beneu, B.; Laval, J.P.; Blanchart, P. Structural transformations of Muscovite at high temperature by X-ray and neutron diffraction. *Appl. Clay Sci.* **2008**, *38*, 259–267. [CrossRef]

24. Fil, B.A.; Özmetin, C.; Korkmaz, M. Characterization and Electrokinetic Properties of Montmorillonite. *Bulg. Chem. Commun.* **2014**, *46*, 258–263.

25. Petit, S.; Righi, D.; Madejová, J. Infrared spectroscopy of NH_4^+-bearing and saturated clay minerals: A review of the study of layer charge. *Appl. Clay Sci.* **2006**, *34*, 22–30. [CrossRef]

26. Du Plessis, P.I.; Gazley, M.F.; Tay, S.L.; Trunfull, E.F.; Knorsch, M.; Branch, T.; Fourie, L.F. Quantification of Kaolinite and Halloysite Using Machine Learning from FTIR, XRF, and Brightness Data. *Minerals* **2021**, *11*, 1350. [CrossRef]

27. Vaculíková, L.; Plevová, E. Identification Of Clay Minerals And Micas In Sedimentary Rocks. *Acta Geodyn. Geomater.* **2005**, *2*, 167–175.

28. Saikia, B.; Parthasarathy, G. Fourier Transform Infrared Spectroscopic Characterization of Kaolinite from Assam and Meghalaya, Northeastern India. *J. Mod. Phys.* **2010**, *1*, 206–210. [CrossRef]

29. Ulian, G.; Moro, D.; Valdrè, G. Infrared and Raman spectroscopic features of clinochlore $Mg_6Si_4O_{10}(OH)_8$: A density functional theory contribution. *Appl. Clay Sci.* **2020**, *197*, 105779. [CrossRef]

30. Patel, H.A.; Somani, R.S.; Bajaj, H.C.; Jasra, V.J. Nanoclays for polymer nanocomposites, paints, inks, greases and cosmetics formulations, drug delivery vehicle and waste water treatment. *Bull. Mater. Sci.* **2006**, *29*, 133–145. [CrossRef]

31. Madejová, J. FTIR techniques in clay mineral studies. *Vib. Spectrosc.* **2003**, *31*, 1–10. [CrossRef]

32. Tironi, A.; Trezza, M.A.; Irassar, E.F.; Scian, A.N. Thermal Treatment of Kaolin: Effect on the Pozzolanic Activity. *Procedia Mater. Sci.* **2012**, *1*, 343–350. [CrossRef]

33. Eren, E.; Afsin, B. An investigation of Cu(II) adsorption by raw and acid-activated bentonite: A combined potentiometric, thermodynamic, XRD, IR, DTA study. *J. Hazard. Mater.* **2008**, *151*, 682–691. [CrossRef] [PubMed]

34. Danková, Z.; Mockovčiaková, A.; Dolinská, S. Influence of ultrasound irradi-ation on cadmium cations adsorption by montmoril-lonite. *Desalin. Water Treat.* **2013**, *52*, 5462–5469. [CrossRef]

35. Qin, Y.; Peng, T.; Sun, H.; Zeng, L.; Zhou, C. Effect of montmorillonite layer charge on the thermal stability of bentonite. *Clays Clay Miner.* **2021**, *69*, 328–338. [CrossRef]

36. Alfonso, P.; Penedo, L.A.; García-Valles, M.; Martinez, S.; Martinez, A.; Trujillo, J.E. Thermal behaviour of kaolinitic raw materials from San José (Oruro, Bolivia). *J. Therm. Anal. Calorim.* **2022**, *147*, 5413–5421. [CrossRef]

37. Smykatz-Kloss, W. Application of differential thermal analysis in mineralogy. *J. Therm. Anal.* **1982**, *23*, 15–44. [CrossRef]